Journal of Magnetic Resonance **145,** 276–290 (2000)
doi:10.1006/jmre.2000.2106, available online at http://www.idealibrary.com on IDEAL®

Finite-Difference Approach for the High-Precision Analysis of Rotating-Frame Diffusion Images

Klaus Woelk,*[,1] Bernd L. J. Zwank,* Peter Trautner,* Edmund Lehnhof,* Joachim Bargon,* Robert J. Klingler,†[,1] Rex E. Gerald II,† and Jerome W. Rathke†

*Institute of Physical and Theoretical Chemistry, University of Bonn, Wegelerstrasse 12, D-53115 Bonn, Germany; and †Chemical Technology Division, Argonne National Laboratory, 9700 South Cass Avenue, Argonne, Illinois 60439

Received November 30, 1999; revised April 12, 2000

DEDICATED TO PROF. DR. GÜNTHER WOELK, TECHNICAL UNIVERSITY OF AACHEN, GERMANY, IN CONSIDERATION OF HIS MANY CONTRIBUTIONHS TO THE NUMERICAL SOLUTION OF PARTIAL DIFFERENTIAL EQUATIONS

A finite-difference approach has been developed for precisely determining diffusion coefficient and T_1 relaxation time in fluid samples analyzed by magnetization-grating rotating-frame imaging (MAGROFI) with either a surface coil or a toroid cavity detector (TCD). This approach avoids shortcomings of phenomenologically based approximations, such as neglect of sample geometries with singularities at the confines of the sample volume, and accounts for the diffusive edge enhancement observed in fluid imaging. Error limits are discussed. The new method has been applied to the determination of the self-diffusion coefficient for MAGROFI experiments using TCDs filled with acetone.

Key Words: **diffusion; rotating-frame imaging; NMR microscopy; magnetization grating; finite difference; toroid cavity.**

INTRODUCTION

This article presents a finite-difference approach that will accurately determine diffusion coefficients from rotating-frame NMR images obtained with toroid cavity detectors (TCDs). Diffusion describes incoherent flow because of Brownian motion; hence, it is the mass transport phenomenon that equilibrates concentration gradients. Since diffusion plays a crucial role in many chemical reactions, phase transitions, and phase-transfer reactions, its determination is fundamental to the understanding of reaction mechanisms and kinetics. Moreover, diffusion limits the accuracy of techniques based on coherent flow, such as chromatography or electrophoresis. Sometimes, however, it is highly desired to improve diffusion pathways, e.g., in methods of medical drug delivery, such as iontophoresis (*1*) or phonophoresis (*2*).

Common NMR methods for measuring diffusion are the PFG (*p*ulsed *f*ield *g*radient) or the PGSE (*p*ulsed-*g*radient *s*pin-*e*cho) technique employing pulsed B_0-field gradients (*3, 4*). Recently, however, several new techniques implementing B_1 gradients have been developed (*5–10*). Among these, a very robust and versatile method is MAGROFI (*ma*gnetization-*g*rating *r*otating-*f*rame *i*maging), developed by Kimmich *et al.* (*10*). Its key element is the simple two-pulse sequence schematically shown in Fig. 1. The first pulse (P1) generates a z-magnetization grating along the direction of the B_1 gradient. During an evolution time (τ), diffusion and relaxation decay the grating, while coherent flow, if present, coherently shifts the positions of its maxima and minima. The second pulse (P2) is part of an RFI (*r*otating-*f*rame *i*maging) procedure that samples the remaining z magnetization with incrementally increased pulse widths (Fig. 1a) (*11*) or with a rapid-imaging pulse train (Fig. 1b) (*12–14*). With the remaining magnetization grating imaged, it is possible to simultaneously evaluate diffusion coefficients, flow velocities, and T_1 relaxation times. Before we describe the new finite-difference approach, we recall and discuss the conventional, phenomenological treatment of MAGROFI with surface coils or, alternatively, with TCDs.

MAGNETIZATION-GRATING ROTATING-FRAME IMAGING

Surface Coil

A surface coil (*15*) exposes the sample to a reasonably uniform B_1 gradient, i.e., to a linearly decreasing B_1 field. If applied on resonance, the pulse P1 of the MAGROFI sequence (duration: t_{P1}) generates a homogeneous yz magnetization helix, in which the magnetization is twisted with a constant pitch along the direction of the B_1 gradient (Fig. 2). According to Bloch's equations, the z component of the helix forms a sinusoidal magnetization grating of

$$M_{z,0}(x) = M_{eq}(x)\cos(-\gamma B_1 t_{P1}) = M_{eq}(x)\cos(-\gamma B_1^0 t_{P1} + k_{P1}x), \quad [1]$$

[1] To whom correspondence should be addressed.

1090-7807/00 $35.00

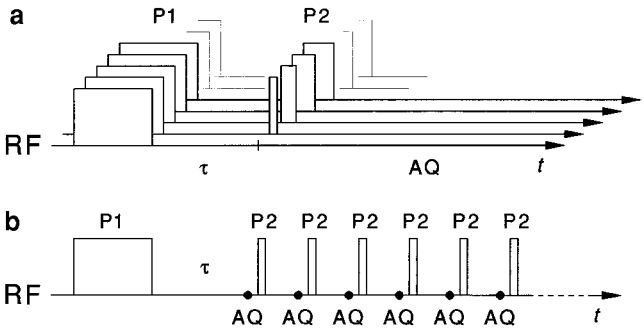

FIG. 1. MAGROFI sequence utilizing (a) the traditional chemical-shift resolved rotating-frame imaging (series of transients with incrementally increasing pulse width) and (b) the rapid-imaging pulse train (single-point acquisition between equal pulses). RF, radiofrequency channel; P1, preparation pulse; τ, evolution time; P2, RFI pulses; AQ, acquisition.

where the subscript zero indicates that no evolution time has past after the preparation pulse P1 was executed. In Eq. [1], $M_{eq}(x)$ is the spatially dependent equilibrium magnetization, γ is the magnetogyric ratio, x is the distance along the center axis perpendicular to the coil's plane, B_1^0 is the virtual B_1 field that would occur at the center of the coil ($x = 0$) if the gradient $G_1 = (\Delta B_1/\Delta x)$ is uniform up to the surface coil's plane, and k_{P1} is the k-space wave number generated with the pulse P1, i.e., $k_{P1} = \gamma G_1 t_{P1}$. In the case of a homogeneous sample, $M_{eq}(x)$ is a constant (M_{eq}). From a rigorous mathematical approach similar to the one of Kimmich *et al.* (*10*), we found that, during the evolution time τ, the grating changes according to

$$M_{z,\tau}(x) = M_{eq}\left[1 - \exp\left(-\frac{\tau}{T_1}\right)\{1 - \exp(-Dk_{P1}^2\tau) \times \cos(-\gamma B_1^0 t_{P1} + k_{P1}x)\}\right], \quad [2]$$

where D is the diffusion coefficient. The cosine term in Eqs. [1] and [2] differs from Kimmich's original equations, in which the origin of the distance scale is placed at the extrapolated point of $B_1 = 0$. Conventionally, however, the origin is positioned at the center of the surface coil, and the phase ($-\gamma B_1^0 t_{P1}$) must be added. Moreover, coherent flow is neglected in the derivation of Eq. [2], since it does not occur in closed, homogeneous samples without convection currents. Because of the principle of reciprocity (*16*), RFI intensities, $I_\tau(x)$, are proportional not only to $M_{z,\tau}(x)$ but also to $B_1(x)$. Thus, if intensity data are acquired by the surface coil that is also used for generating the grating, $I_\tau(x)$ must be multiplied by x to yield information about $M_{z,\tau}(x)$. In contrast, Canet *et al.* (*6*) used a separate Helmholtz saddle coil for data acquisition exhibiting a homogeneous B_1 field along the sample, and no signal intensity correction was necessary. Note, however, that all signal intensities are relative numbers regardless of the acquisition procedure, and that they must be scaled by a standard if needed.

In addition to T_1 relaxation, Eq. [2] represents an exact and complete solution of Fick's second law of diffusion, $(\partial c/\partial t) = D(\partial^2 c/\partial x^2)$, if

(a) Eq. [1] is a boundary condition (starting condition),
(b) the gradient G_1 along the sample is strictly uniform,
(c) the sample evenly expands perpendicular to the gradient G_1, and
(d) the sample is homogeneous and contains no singularities along the gradient.

For surface coils, prerequisites (a) through (d) are fulfilled only to a certain extent. For example, the assumption of a uniform gradient, G_1, is an approximation (*10*). Additionally, singularities exist at the walls of the sample container, where diffusion is restricted toward the inside of the sample. Consequently, an effect known as diffusive edge enhancement in fluid imaging (*17*) is observed. If areas of edge enhancement are evaluated for diffusion using the phenomenological approach of Eq. [2], coefficients are extracted, which are considerably smaller than the true diffusion coefficient. These ill-determined coefficients have been termed "effective," "apparent" (*18*), or "localized" (*19*) diffusion coefficients but do not reflect the physics present in the sample. Hence, edge enhancement is not the result of local changes in the diffusion coefficient but simply caused by the presence of singularities such as sample boundaries. Furthermore, because the area of edge enhancement depends upon the evolution period τ of the NMR sequence, apparent diffu-

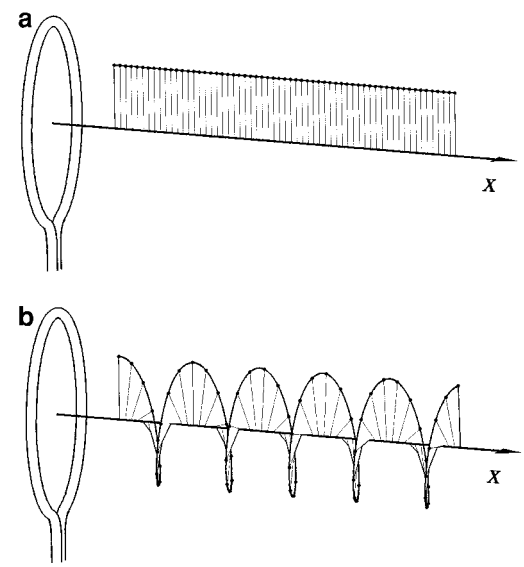

FIG. 2. Magnetization grating generated by a single radiofrequency (RF) pulse applied to a surface coil. Within the surface coil's uniform B_1 gradient, the RF pulse rotates the equilibrium magnetization (a) into a helix (b) along the distance axis x, i.e., into a sinusoidal magnetization grating. Magnetization vectors along the x axis are symbolized by straight pins, in which each head depicts the tip of a vector.

sion coefficients are strongly influenced by the time frame of the experiment, and even come out negative sometimes. Utilizing the more meticulous mathematical approach of finite differences, however, we show that edge enhancement is solely defined by regular diffusion.

Nevertheless, surface-coil MAGROFI is a robust new technique for determining diffusion coefficients when data from the center of a sample are evaluated with Eq. [2]. Because the technique consists of a simple two-pulse sequence, in which no B_0 gradients are switched, the precision of determination is similar to, if not better than, that of other NMR methods. The accuracy of a diffusion coefficient determined by surface-coil MAGROFI depends, among other factors, on

(a) how well defined and strong the uniform gradient, G_1, is,
(b) how accurately its value can be determined, and
(b) how many experiments are used for the evaluation.

A MAGROFI experiment that utilizes a uniform B_1 gradient, such as the gradient of a surface coil, delivers only one data point for a linear regression of amplitudes versus evolution time (*10*) or, alternatively, versus *k*-space wave number. Accordingly, multiple MAGROFI experiments must be recorded to determine a single diffusion coefficient. Because of the linear-regression procedure, the standard deviation of the diffusion coefficient decreases proportional to $(N - 2)$, where N is the number of experiments.

In the following, we discuss the use of nonuniform B_1 gradients for MAGROFI measurements, and show how a diffusion coefficient is extracted from multiple data points of a single MAGROFI experiment.

Toroid Cavity Detector

While TCD B_1 gradients are not uniform, they are mathematically well defined (*20*) by

$$B_1(r) = \frac{A}{r} \quad \Rightarrow \quad \frac{dB_1(r)}{dr} = -\frac{A}{r^2}, \qquad [3]$$

where A is the so-called "torus factor," i.e., the proportionality constant between B_1 and r^{-1}. Near the central conductor of TCDs, B_1 gradients are typically much stronger than those of surface coils. We have achieved gradients of 6–8 mT/mm (600–800 G/cm) using conventional NMR transmitter equipment (H band, 100 W; X band, 300 W). For this reason, and because of the high accuracy to which the gradient is defined, toroid cavity MAGROFI should, in general, yield diffusion coefficients that are more accurate. According to Eq. [3], the pulse P1 generates a magnetization helix with decreasing pitch directed radially from the central conductor of a TCD (i.e., along the radial dimension r in Fig. 3). The radially dependent, asymmetric z-magnetization grating, $M_{z,0}(r)$, of this pulse is described by

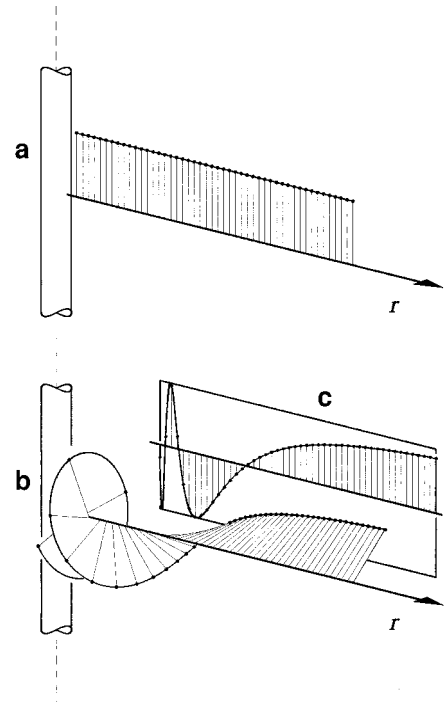

FIG. 3. Magnetization grating generated by a single RF pulse applied to a toroid cavity detector. The central conductor of the toroid cavity is symbolized by the vertical rod in each plot, while straight pins exemplify the magnetization vectors. Because of the nonuniform B_1 gradient, the RF pulse rotates the equilibrium magnetization (a) into a helix (b) with a high pitch close to the central conductor and a lower pitch further away. The z component of the helix (c) reveals a nonuniform z-magnetization grating. The evolution of this grating is used for the determination of diffusion and T_1 relaxation.

$$M_{z,0}(r) = M_{eq}\cos\left(-\frac{\gamma A t_{P1}}{r}\right). \qquad [4]$$

Figure 4a shows data points (circles) from a grating sampled by toroid cavity MAGROFI with the evolution time, τ, set to zero. The rotating-frame imaging intensities, $I(r)$, obtained from the experiment have been divided by r^2 to yield radially dependent magnetization data, $M_{z,0}(r)$. This scaling procedure was outlined in detail before (*20*). Note that an approach similar to that of Canet *et al.* (*6*), where the scaling of intensities is not required because the data are sampled by a separate coil of homogeneous B_1 field (Helmholtz saddle coil), cannot be conducted with TCDs.

Whenever the evolution time, τ, is smaller than five times the relaxation time constant T_2, undesired *xy* magnetization remains at the time when P2 is started. This unwanted, transverse magnetization is canceled by accumulating multiples of two transients for each RFI spectrum, in which the phase of P1 is cycled by 180° versus P2, or multiples of four, in which the phase of P1 is cycled by 90° versus P2. A simulation of the grating was conducted with Eq. [4] and fitted to data from an experiment with acetone at room temperature, refining A and

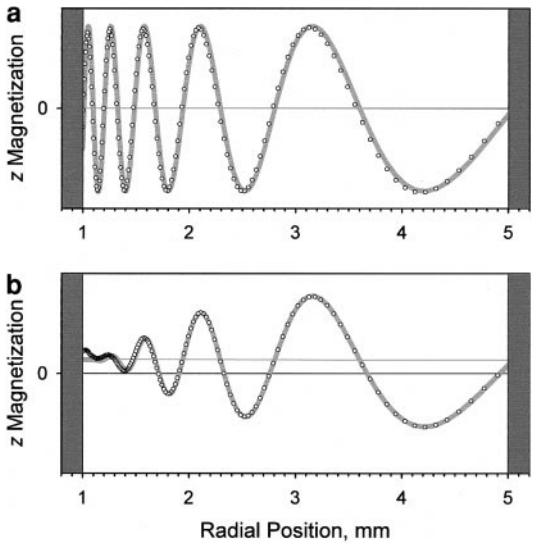

FIG. 4. Plot of experimental RFI intensities (circles) versus radial distance obtained from toroid cavity MAGROFI experiments on a homogeneous sample of acetone ($t_{P1} = 212$ μs, $n = 512$, $\Delta t_{P2} = 12$ μs, $A = 0.6934 \pm 0.0014$ mT mm). Dark gray, vertical bars represent the sample confines at $r_{min} = 1.0$ mm (central conductor) and at $r_{max} = 5.0$ mm (outer wall) of the toroid detector. In (a), the evolution time, τ, was set to zero, so that no decay of the grating occurred. In (b), the evolution time was set to $\tau = 1.0$ s, and decay of the grating because of diffusion is clearly visible. The thin, horizontal line shows the baseline offset caused by T_1 relaxation. In both plots, the heavy gray line represents the best fit of Eq. [5] to the experimental data ($D = 4.72 \times 10^{-9}$, $T_1 = 5.45$ s).

M_{eq}. In Fig. 4a, the best fit is shown as a solid, heavy gray line. Similarly, the grating was sampled after an evolution time of $\tau = 1.0$ s (Fig. 4b). Evolution of the grating can be reproduced mathematically by (*21*)

$$M_{z,\tau}(r) = M_{eq}\left[1 - \exp\left(-\frac{\tau}{T_1}\right)\left\{1 - \exp\left(-\frac{D\gamma^2 A^2 t_{P1}^2 \tau}{r^4}\right) \times \cos\left(-\frac{\gamma A t_{P1}}{r}\right)\right\}\right]. \quad [5]$$

Because of the distinctive B_1 gradient, a z-magnetization grating formed in a TCD exhibits a wide range of k-space wave numbers. Thus, a single MAGROFI experiment is sufficient for extracting the diffusion coefficient and the T_1 relaxation time constant from a three-parameter fit of Eq. [5], refining M_{eq}, D, and T_1. If only two transients are utilized to cancel remaining transversal magnetization (phase cycling by 180° of P1 versus P2) and, in addition, rapid imaging by a pulse train (*12–14*) is used as the RFI procedure (Fig. 1b), a TCD MAGROFI experiment is conducted in less than a minute of experimental time. The torus factor, A, derived from the experiment in Fig. 4a was used for the simulation in Fig. 4b, since both the sample and all parameters but the evolution time were kept the same during the two experiments. In Fig. 4b, the best fit is also shown as a solid, heavy gray line. For the room-temperature acetone sample used in the experiment, the fit returns a diffusion coefficient of $4.72 \times 10^{-9} \pm 0.20 \times 10^{-9}$ m^2 s^{-1} ($\pm 4.2\%$) and a T_1 relaxation time of 5.45 ± 0.11 s ($\pm 1.9\%$). For comparison, a room-temperature diffusion coefficient of 4.77×10^{-9} m^2 s^{-1} is reported in the literature (*22*). In toroid cavity MAGROFI, the standard deviation of diffusion-coefficient measurements decreases with the number of data points that fall inside the TCD. This number of data points is optimized by properly choosing the pulse-width increment, Δt_{P2}, and is increased with the number of spectra, n, recorded in the RFI procedure (*20*).

While Eq. [5] provides a reasonable phenomenological description, it is not an exact solution of Fick's laws of diffusion, but an approximation that was derived by modifying Eq. [2]. In contrast to the case with uniform gradients, no mathematically exact, analytical solution is known to reproduce the evolution of gratings in TCDs, not even inside the sample remote from the impermeable boundaries at the central conductor and the outer wall of the cavity. Accordingly, although the B_1 gradient is well defined and usually stronger compared with surface coils, the evaluation of diffusion coefficients with Eq. [5] involves approximations that increase the determination error. To take advantage of well-defined, strong, and nonuniform gradients while avoiding the use of phenomenological approximations, we developed an iterative, numerical finite-difference procedure that reproduces the evolution of asymmetric gratings more accurately. With this new approach, rotating-frame images of MAGROFI experiments can be described regardless of the detector's geometry or the sample's singularities and homogeneity.

FINITE-DIFFERENCE APPROACH

Finite-difference calculations are numerical procedures commonly used to solve systems of partial differential equations with complex boundary conditions, especially when time progress cannot be reproduced easily and precisely with phenomenological equations. For finite-difference procedures, the spatial range, area, or volume under investigation is divided into a finite number of intervals, fields, or volume elements, respectively (Δx in Fig. 5). The elements are characterized by single, distinct function values optimally acquired from the interval's midpoints. For each function value [$f(a)$, $f(a + 1)$, . . . , $f(k - 1)$, $f(k)$, $f(k + 1)$, . . . , $f(z - 1)$, $f(z)$ in Fig. 5], the time-dependent differential equation is solved individually. Either neighboring data or, at singularities (a and z in Fig. 5), additional function information such as the impermeability of sample confines is included to serve as a boundary condition for the calculation. The result is a set of new function values for an advanced but limited time step, Δt. The time step width must meet stability conditions, discussed later.

In some fields of scientific research, finite-difference calculations have become widespread for simulating transport phe-

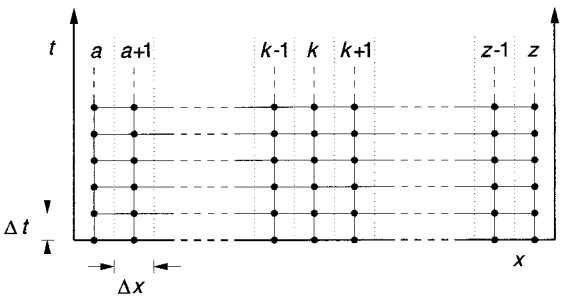

FIG. 5. Diagram illustrating the principle of conventional finite-difference propagation. The spatial dimension of interest is divided into equal intervals, Δx. Function values (filled circles) of the intervals are individually progressed by finite time steps, Δt. Neighboring values or other function information (e.g., sample confines) is used as boundary conditions.

nomena. In electrochemistry, for example, finite-difference calculations are often included in computer software packages for analyzing near-electrode processes. For imaging molecular motion by NMR, however, evaluations based on the propagator theory (*4*) are common. Nevertheless, we preferred the finite-difference simulation for analyzing magnetization gratings in TCDs because it is able to accurately reproduce the effects of diffusion in the bulk sample and close to impermeable boundaries or other singularities.

Finite-difference equations for solving standard propagation problems are introduced in many textbooks. Nevertheless, we present a detailed derivation of TCD finite-difference equations, since it differs from conventional one-dimensional approaches (Fig. 5). In these conventional approaches, Cartesian coordinates with uniform planar volume elements ($\partial V/\partial x$ = const.) and equally distributed data points (Δx = const.) are assumed, while the cylindrical symmetry of TCDs requires cylindrical coordinates with the consequence that the experimental data are distributed unevenly on the radial distance axis (*20, 23*).

Derivation of Finite-Difference Equations

A common approach for obtaining finite-difference equations is the use of Taylor's expansion theorem (*24*). For equidistant intervals and Cartesian coordinates, the leading term neglected is usually second order in distance squared between two data points and sufficiently small. For an uneven distribution of intervals on the radial axis in cylindrical coordinates, however, determining the error terms is more cumbersome. If simply the same expansion-theorem approach is used, the leading error term can increase up to first order in distance. Thus, to avoid the dilemma of undefined or unreasonably large error terms, we prefer to solve the diffusion problem by analogy to an electric circuit model that has been utilized extensively in heat-flow calculations (*25*) but has been mentioned only occasionally with respect to diffusion measurements (*26, 27*). The analogy was introduced by Beuken (*28*), who invented electric analogue machines to study complicated transport phenomena. Digital modeling of these analogue machines (*29*) revealed that the maximum error of computing is significantly reduced compared with straight finite-difference methods (*30*). In principle, the model is based on the identity between equations of transport phenomena and those governing electric ladder networks. It allows the mathematical treatment of a resistor and capacitor (RC) ladder network to be employed for MAGROFI diffusion experiments by substituting z magnetization for voltage, diffusion coefficients for conductivity, and sample volume for capacitance. Figure 6 shows how an RC network is assembled to serve as an analogue model for the uneven distribution of function values in cylindrical TCDs. Since voltages (u_k) represent local z magnetizations ($M_{z,k}$), it is important to know the radial positions r_k represented by the experimental data points k. These positions are obtained from processing the RFI intensities of the toroid cavity MAGROFI experiment.

To yield spatial information from RFI experiments, a series of spectra acquired with incrementally increasing pulse widths (Fig. 1a) is transformed by a second, real-data Fourier transformation (*11, 20, 23*). Alternatively, the intensities obtained by the rapid-imaging pulse train (Fig. 1b) are directly converted by a real-data Fourier transformation (*12–14*). From both approaches, a set of intensities versus nutation frequency is derived. The nutation frequencies, ν_1, are spaced evenly by $(-n\Delta t_{P2})^{-1}$, where n is the number of pulse-width-dependent experiments. They range from $\nu_{1,\min} = 0$ Hz to the frequency below $\nu_{1,\max} = (-2\Delta t_{P2})^{-1}$, i.e., the Nyquist frequency. The Nyquist frequency is determined by the pulse-width increment, Δt_{P2}, of the RFI experiment but is not included as a data point. Thus,

$$\nu_{1,k} = -\frac{k}{n\Delta t_{P2}}, \quad k = 0, 1, \ldots, \frac{n}{2} - 1. \qquad [6]$$

Since $2\pi\nu_1 = -\gamma B_1$ and $B_1 = A/r$ (Eq. [3]), nutation frequencies of TCD experiments are transformed into radially dependent data at

$$r_k = \frac{\gamma A n \Delta t_{P2}}{2\pi k}, \quad k = 1, 2, \ldots, \frac{n}{2} - 1. \qquad [7]$$

Because $r_0 = \infty$, the radius of $k = 0$ is omitted from subsequent calculations. Equations [6] and [7] indicate that TCD nutation data are evenly distributed in frequency space but unevenly distributed in real space.

To compare experimental data with finite-difference simulations, we divided the TCD's radial coordinate into intervals (Δr_k) that are characterized by function values at r_k. Consequently, Δr_k ranges from $r_{k+1/2}$ to $r_{k-1/2}$:

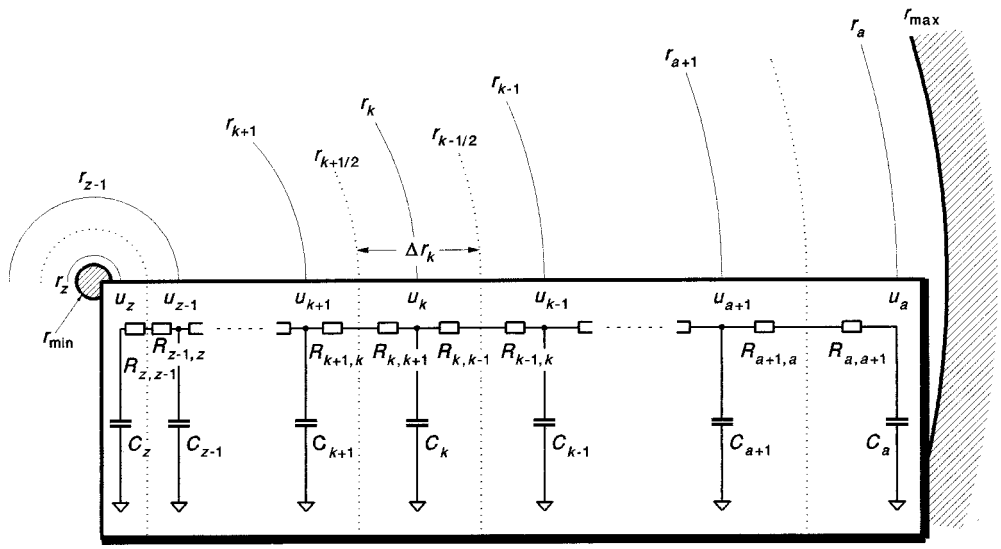

FIG. 6. Electric currents in an RC ladder network are used as an analogue model for the transport of magnetization in toroid cavity detectors. The voltages across capacitors and the magnetizations of volume elements are governed by the same mathematical relationship. Accordingly, capacitors (C_k) are identified with cylindrical-shell volume elements (V_k), voltages (u_k) with magnetizations (M_k), and the reciprocal of the resistivity (κ^{-1}), i.e., the conductivity, with the diffusion coefficient.

$$\Delta r_k = r_{k-1/2} - r_{k+1/2} = \frac{\gamma A n \Delta t_{P2}}{2\pi(k^2 - \frac{1}{4})}. \qquad [8]$$

Note that $r_{k+1/2}$ is smaller than $r_{k-1/2}$, and Δr_k decreases as k increases. Accordingly, the size of the intervals is small near the central conductor and increases to the outer wall of the cavity. If the distribution of experimental data points is too coarse to accurately describe the magnetization profile, it might become necessary to subdivide each Δr_k region further by placing additional, virtual data points between r_k and r_{k+1}. For most of our data sets, however, the preparation pulse width (t_{P1}) was small compared to the maximum imaging pulse width ($t_{P1} \leq \frac{1}{4} n \Delta t_{P2}$); accordingly, the spatial separation of the data points was sufficiently fine to map the distance between two adjacent z-magnetization extrema with at least two experimental data points.

As shown in Fig. 6, capacitors C_k are located at the radii r_k (Eq. [7]) and function as storage devices for electric charge. In the analogy with z-magnetization transport by diffusion, capacitors (C_k) represent volume elements (V_k) that cover the intervals Δr_k of Eq. [8], i.e., consist of cylindrical shells with an inner radius of $r_{k+1/2}$ and an outer radius of $r_{k-1/2}$,

$$V_k = \pi h(r_{k-1/2}^2 - r_{k+1/2}^2), \qquad [9]$$

where h is the height of the sample volume inside the TCD. The capacitors C_a and C_z in Fig. 6 are those closest to the outer and inner radial confines of the sample volume, respectively. Their volume analogues, V_a and V_z, adjoin the outer wall at r_{max} and the central conductor at r_{min},

$$V_a = \pi h(r_{max}^2 - r_{a+1/2}^2), \quad V_z = \pi h(r_{z-1/2}^2 - r_{min}^2), \qquad [10]$$

where a and z indicate the data points closest to the outer wall and the central conductor, respectively. Note that V_a or V_z only cover volume inside the TCD, although r_a or r_z are sometimes outside of the sample volume.

In the analogue model of Fig. 6, transport of z magnetization between volume elements to equilibrate magnetization gradients is identified with electric current between capacitors to equilibrate differences in voltage. The current $i_{k,k-1}$ between C_k and C_{k-1} is given by Ohm's law,

$$i_{k,k-1} = \frac{u_k - u_{k-1}}{R_{k,k-1} + R_{k-1,k}}, \qquad [11]$$

where $R_{k,k-1}$ and $R_{k-1,k}$ are the resistors between the capacitors C_k and C_{k-1}. This notation indicates that, for example, $R_{k,k+1}$ is connected to C_k in the direction of C_{k+1}. From an initial distribution of voltages across the capacitors, u_k changes according to

$$C_k \frac{du_k}{dt} = i_{k+1,k} - i_{k,k-1} = \frac{u_{k+1} - u_k}{R_{k+1,k} + R_{k,k+1}} - \frac{u_k - u_{k-1}}{R_{k,k-1} + R_{k-1,k}}, \qquad [12]$$

where the sign of i is positive, if current runs from smaller to

larger radii, i.e., from the center of the torus to the outside. In Eq. [12], the analogy of the RC ladder network to the diffusion problem is readily seen, when the flow of electrons (i.e., current) is identified with the flow of matter. Using the additional analogies of voltage with concentration and conductivity (i.e., reciprocal resistivity) with the diffusion coefficient, Fick's first law of diffusion results.

Since no current crosses the boundaries at $r_{\max}$ and $r_{\min}$ in Fig. 6, voltages across C_a and C_z change according to

$$C_a \frac{du_a}{dt} = \frac{u_{a+1} - u_a}{R_{a+1,a} + R_{a,a+1}}, \quad C_z \frac{du_z}{dt} = -\frac{u_z - u_{z-1}}{R_{z,z-1} + R_{z-1,z}}. \tag{13}$$

In electrotechnology, resistance R along a distance x is defined as

$$R = \int \frac{\kappa}{S(x)}\, dx, \tag{14}$$

where κ is the resistivity, and $S(x)$ is the area through which the current passes. In the cylindrical geometry of TCDs, the area S is a cylindrical surface that depends upon the radius, i.e., $S(r) = 2\pi rh$. Assuming uniform resistivity across each interval Δr_k, the resistors $R_{k,k-1}$ and $R_{k,k+1}$ are determined by

$$R_{k,k-1} = \frac{\kappa_k}{2\pi h} \ln\left(\frac{r_{k-1/2}}{r_k}\right), \quad R_{k,k+1} = \frac{\kappa_k}{2\pi h} \ln\left(\frac{r_k}{r_{k-1/2}}\right). \tag{15}$$

Since, in Beuken's model, diffusion is equivalent to conductance in electric networks, the diffusion coefficient D is identified with the conductivity, i.e., the reciprocal of resistivity, κ^{-1}. Equation [12] and the analogies of C_k with V_k, u_k with $M_{z,k}$, and D with κ^{-1} provide the differential equation for irregular intervals in TCDs,

$$V_k \frac{dM_{z,k}}{dt} = \frac{M_{z,k+1} - M_{z,k}}{\frac{1}{2\pi hD_{k+1}} \ln\left(\frac{r_{k+1/2}}{r_{k+1}}\right) + \frac{1}{2\pi hD_k} \ln\left(\frac{r_k}{r_{k+1/2}}\right)} - \frac{M_{z,k} - M_{z,k-1}}{\frac{1}{2\pi hD_k} \ln\left(\frac{r_{k-1/2}}{r_k}\right) + \frac{1}{2\pi hD_{k-1}} \ln\left(\frac{r_{k-1}}{r_{k-1/2}}\right)}. \tag{16}$$

Substitution with Eqs. [7], [8], and [9] leads to

$$\frac{dM_{z,k}}{dt} = \frac{1}{k(\Delta r_k)^2} \left[\frac{M_{z,k+1} - M_{z,k}}{\frac{1}{D_{k+1}} \ln\left(\frac{k+1}{k+\frac{1}{2}}\right) + \frac{1}{D_k} \ln\left(\frac{k+\frac{1}{2}}{k}\right)} - \frac{M_{z,k} - M_{z,k-1}}{\frac{1}{D_k} \ln\left(\frac{k}{k-\frac{1}{2}}\right) + \frac{1}{D_{k-1}} \ln\left(\frac{k-\frac{1}{2}}{k-1}\right)} \right]. \tag{17}$$

During a finite period Δt, the magnetizations $M_{z,k}$ change from $M_{z,k,t}$ to $M_{z,k,t+\Delta t}$. A linear approximation of Eq. [17] yields the general, explicit finite-difference equation for TCDs,

$$M_{z,k,t+\Delta t} = M_{z,k,t} + \frac{\Delta t}{k(\Delta r_k)^2} \times \left[\frac{M_{z,k+1,t} - M_{z,k,t}}{\frac{1}{D_{k+1}} \ln\left(\frac{k+1}{k+\frac{1}{2}}\right) + \frac{1}{D_k} \ln\left(\frac{k+\frac{1}{2}}{k}\right)} - \frac{M_{z,k,t} - M_{z,k-1,t}}{\frac{1}{D_k} \ln\left(\frac{k}{k-\frac{1}{2}}\right) + \frac{1}{D_{k-1}} \ln\left(\frac{k-\frac{1}{2}}{k-1}\right)} \right]. \tag{18}$$

If diffusion is independent of radial position, a single diffusion coefficient D can be introduced, and Eq. [18] simplifies to

$$M_{z,k,t+\Delta t} = M_{z,k,t} + \frac{D\Delta t}{k(\Delta r_k)^2} \times \left[\frac{M_{z,k+1,t} - M_{z,k,t}}{\ln\left(\frac{k+1}{k}\right)} - \frac{M_{z,k,t} - M_{z,k-1,t}}{\ln\left(\frac{k}{k-1}\right)} \right]. \tag{19}$$

Equation [19] is the finite-difference equation that computes changes of radially distributed z magnetization in homogeneous TCD samples. The equation contains all the characteristics of TCDs and, in addition, of the RFI sampling therein. Accordingly, natural logarithm terms occur in Eq. [19] as a result of integrating across differential volume elements in cylindrical geometry (Eq. [14]). Furthermore, the FFT (*f*ast *F*ourier *t*ransform) algorithm applied to RFI data and the special relationship between the B_1 field (thus, nutation frequency) and radial distance in TCDs (Eq. [3]) cause the logarithm terms to contain only data-point indices (k) as variables rather than radial distances (r_k).

For large data-point indices (e.g., $k > 500$), the terms $k \ln[(k+1)/k]$ and $k \ln[k/(k-1)]$ both approach unity, and

Eq. [19] transforms into the well-known finite-difference equation of planar sheets (*24*):

$$M_{z,k,t+\Delta t} = M_{z,k,t} + \frac{D\Delta t}{(\Delta r_k)^2}(M_{z,k+1,t} - 2M_{z,k,t} - M_{z,k-1,t}). \quad [20]$$

Accordingly, differences between individual calculations with Eq. [19] and those with Eq.[20] can be quite small, even if Eq. [20] is applied to the cylindrical coordinates of TCDs. To compute significant time advancements, however, individual finite-difference calculations must be repeated many times and rapidly increasing cumulative errors occur. Hence, we prefer to use Eq. [19] because it is more accurate.

Equations [18] and [19] represent explicit finite-difference equations that calculate the evolution of an initial radial distribution of magnetization in the cylindrical sample geometry of TCDs. For computer automation of the finite-difference calculation, however, it is common practice to separate the terms that involve $M_{z,k+1}$, $M_{z,k}$, or $M_{z,k-1}$. Accordingly, Eq. [19] yields

$$\begin{aligned} M_{z,k,t+\Delta t} &= M_{z,k+1,t}\left[\frac{D\Delta t}{k(\Delta r_k)^2}\frac{1}{\ln\left(\frac{k+1}{k}\right)}\right] + M_{z,k,t} \\ &\quad \times\left[1 - \frac{D\Delta t}{k(\Delta r_k)^2}\left(\frac{1}{\ln\left(\frac{k+1}{k}\right)} + \frac{1}{\ln\left(\frac{k}{k-1}\right)}\right)\right] \\ &\quad + M_{z,k-1,t}\left[\frac{D\Delta t}{k(\Delta r_k)^2}\frac{1}{\ln\left(\frac{k}{k-1}\right)}\right] \\ &= M_{z,k+1,t}p_{k+1} + M_{z,k,t}p_k + M_{z,k-1,t}p_{k-1}. \end{aligned} \quad [21]$$

For the data points a and z adjacent to the inner and outer confines of the sample volume, equations similar to Eq. [21] are derived based on Eqs. [10] and [13]:

$$\begin{aligned} M_{z,a,t+\Delta t} &= M_{z,a+1,t}\left[\frac{2D\Delta t}{r_{\max}^2 - r_{a+1/2}^2}\frac{1}{\ln\left(\frac{a+1}{a}\right)}\right] \\ &\quad + M_{z,a,t}\left[1 - \frac{2D\Delta t}{r_{\max}^2 - r_{a+1/2}^2}\frac{1}{\ln\left(\frac{a+1}{a}\right)}\right] \\ &= M_{z,a+1,t}p_{a+1} + M_{z,a,t}p_a, \end{aligned}$$

$$\begin{aligned} M_{z,z,t+\Delta t} &= M_{z,z,t}\left[1 - \frac{2D\Delta t}{r_{z-1/2}^2 - r_{\min}^2}\frac{1}{\ln\left(\frac{z}{z-1}\right)}\right] \\ &\quad + M_{z,z-1,t}\left[\frac{2D\Delta t}{r_{z-1/2}^2 - r_{\min}^2}\frac{1}{\ln\left(\frac{z}{z-1}\right)}\right] \\ &= M_{z,z,t}p_z + M_{z,z-1,t}p_{z-1}. \end{aligned} \quad [22]$$

For further simplification, Eqs. [21] and [22] are combined and transformed into matrix notation. Accordingly,

$$\begin{pmatrix} M_{z,a,t+\Delta t} \\ \cdots \\ M_{z,k,t+\Delta t} \\ \cdots \\ M_{z,z,t+\Delta t} \end{pmatrix} = \begin{pmatrix} p_a & p_{a+1} & & & 0 \\ & \cdots & & & \\ & p_{k-1} & p_k & p_{k+1} & \\ & & & \cdots & \\ 0 & & & p_{z-1} & p_z \end{pmatrix} \begin{pmatrix} M_{z,a,t} \\ \cdots \\ M_{z,k,t} \\ \cdots \\ M_{z,z,t} \end{pmatrix}. \quad [23]$$

Put another way, $\mathbf{M}_{z,t+\Delta t}(r) = P\mathbf{M}_{z,t}(r)$, where $\mathbf{M}_{z,t}(r)$ and $\mathbf{M}_{z,t+\Delta t}(r)$ are z-magnetization distributions before and after the application of the diagonal propagation band matrix P, respectively. The matrix P consists of the multipliers p_x from Eqs. [21] and [22]. With Eq. [23], the evolution of z magnetization in TCDs is calculated for the finite period Δt. To follow magnetization gratings through the entire evolution time τ, the propagation matrix P must be applied multiple times starting with the initial grating, $\mathbf{M}_{z,0}(r)$, of Eq. [4]. Hence,

$$\mathbf{M}_{z,\tau}(r) = P^H\mathbf{M}_{z,0}(r), \quad [24]$$

where H is the number of propagation steps; i.e., $H = \tau/\Delta t$. In a homogeneous sample, the equilibrium magnetization M_{eq} is uniform, and Eq. [24] can be normalized, yielding

$$\mathbf{M}^0_{z,\tau}(r) = P^H\mathbf{M}^0_{z,0}(r), \quad [25]$$

where $\mathbf{M}^0_{z,\tau}(r) = \mathbf{M}_{z,\tau}(r)/M_{eq}$ and $\mathbf{M}^0_{z,0}(r) = \mathbf{M}_{z,0}(r)/M_{eq}$. The normalized, initial grating $\mathbf{M}^0_{z,0}(r)$ is obtained from the cosine term of Eq. [4]. With Eq. [25], progression of a magnetization profile in TCDs is calculated without explicit knowledge of M_{eq}.

Convergence

Finite-difference approaches are numerical calculations intended to deliver results as close as possible to the true solutions of partial differential equations. They are assumed "compatible" if the errors become zero as the finite differences in space, Δr_k, and time, Δt, both approach zero. Furthermore, they are called "stable" if the introduction of additional, smaller steps in space or time does not increase the cumulative round-off error (*31*). In addition, it is important to watch whether or not the finite-difference procedure converges. Since the step widths in space and time are interdependent, both can be too large to converge: as a result, oscillations with increasing errors occur. In TCD experiments, finite differences in

space, Δr_k, are predetermined by the experimental data points (Eq. [8]). Therefore, the mandatory condition of convergence limits the maximum, normalized time step, $D\Delta t$.

The finite time step, Δt, which was introduced in Eq. [18], evolved from a linear approximation of Eq. [17]. The approximation is valid if particles from volume elements V_k interfere only with neighboring volume elements, V_{k-1} or V_{k+1}, but not with V_{k-2} or V_{k+2}. Thus, during Δt, particles should not travel further than the smallest Δr of all volume elements. The root mean square distance, $\bar{x}$, that particles travel in one spatial dimension by random walk is given by the Einstein–Smoluchowski relation (*32*)

$$\bar{x} = \sqrt{2D\Delta t} \quad \Rightarrow \quad D\Delta t = \frac{\bar{x}^2}{2}. \qquad [26]$$

According to Eq. [8], Δr_k decreases as k increases, and the smallest Δr_k of all data points inside the TCD should be the one closest to the central conductor; i.e., $\Delta r_z = r_{z-1/2} - r_{\min}$. However, because of the fixed confines, $r_{\max}$ and $r_{\min}$, of the sample volume, the interval $\Delta r_a = r_{\max} - r_{a+1/2}$ can, in principle, be smaller than Δr_z, and an individual test must be conducted. Additionally, the computer program must determine whether Δr_a and Δr_z are large enough to be included in the calculation. If either one is within the range of the square root of the computer's round-off error, it should be omitted. Without this determination, Δr_a or Δr_z and, according to Eq. [26], $D\Delta t$ can approach zero. Finally, the smallest interval that is actually included in the finite-difference simulation is used to determine the maximum normalized time step $D\Delta t$. It should be set to a maximum of 80–90% of the value calculated by Eq. [26] to ensure that the finite-difference procedure remains stable and converges even if there are severe round-off errors. In finite-difference calculations, the convergence criterion discussed here is generally known as the Courant–Friedrichs–Lewy criterion or, in short, the Courant criterion (*33*).

SIMULATIONS

Diffusion

Based on the finite-difference matrix expression of Eq. [25] and under the consideration of the Courant criterion, the evolution of z-magnetization gratings in TCDs was calculated and compared to results from the phenomenological expression given by Eq. [5]. Figure 7 shows simulated magnetization profiles after several, normalized evolution times, $D\tau/(r_{\min})^2$, obtained for a TCD of normalized radii ($r/r_{\min}$) with $r_{\min} = 1$ and $r_{\max} = 5$. To show the influence of diffusion alone, we neglected T_1 relaxation in the profiles of Fig. 7. Consequently, the long-term evolution profile [$D\tau/(r_{\min})^2 = \infty$, Fig. 7c] differs from the equilibrium magnetization reached after about five times T_1. However, it also deviates from collapsing all

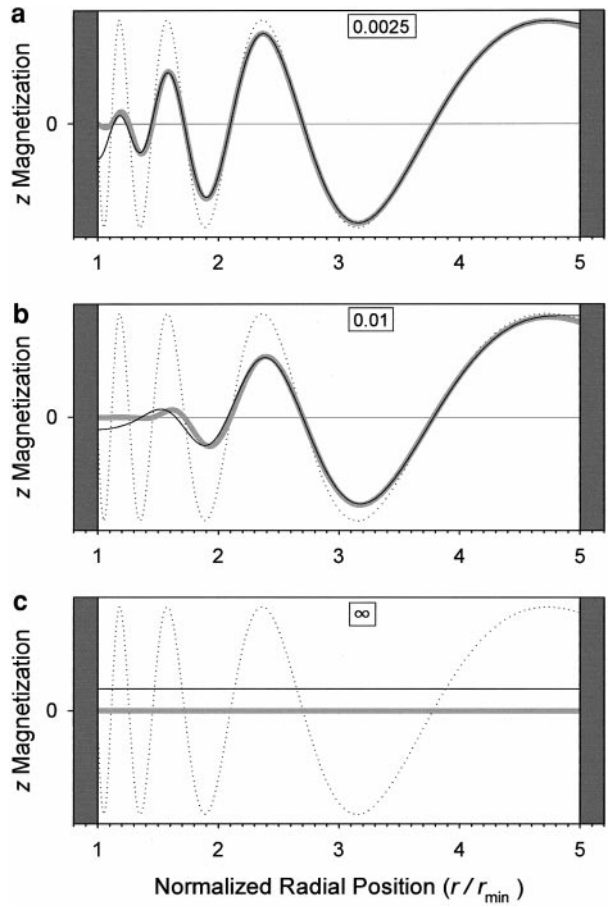

FIG. 7. Decay of a toroid cavity z-magnetization grating according to finite-difference calculations (solid black lines) and calculations from the phenomenological approach (heavy gray lines) after the normalized evolution times of (a) $D\tau/(r_{\min})^2 = 0.0025$, (b) $D\tau/(r_{\min})^2 = 0.01$, and (c) $D\tau/(r_{\min})^2 = \infty$. The dotted lines show the initial grating generated by the preparation pulse, while the dark gray, vertical bars indicate the sample confines at $r/r_{\min} = 1$ and $r/r_{\min} = 5$. To exclusively show the effects of diffusion, we neglected T_1 relaxation in the calculation.

magnetization to zero as predicted by Eq. [5] with $T_1 = \infty$. Because of the impermeable boundaries at $r_{\min}$ and $r_{\max}$, diffusion is limited to within the sample volume, and magnetization is equilibrated to the average sample magnetization of the initial grating.

Two additional findings distinguish the results of the finite-difference calculation from the predictions of Eq. [5]. First, the data in Fig. 7 demonstrate that diffusion not only dampens oscillations of the grating but also shifts its extrema to smaller radii. This effect has been observed earlier (*21*) and is especially noticeable at the profile of $D\tau/(r_{\min})^2 = 0.01$ in Fig. 7b. Consequently, when using Eq. [5], one must restrict the analysis to grating extrema that are not smaller than 10% of the initial value at $\tau = 0$ (*21*). This fundamental difference between the two calculational methods is not simply an artifact caused by impermeable sample boundaries. The comparison demonstrates that Eq. [5] is

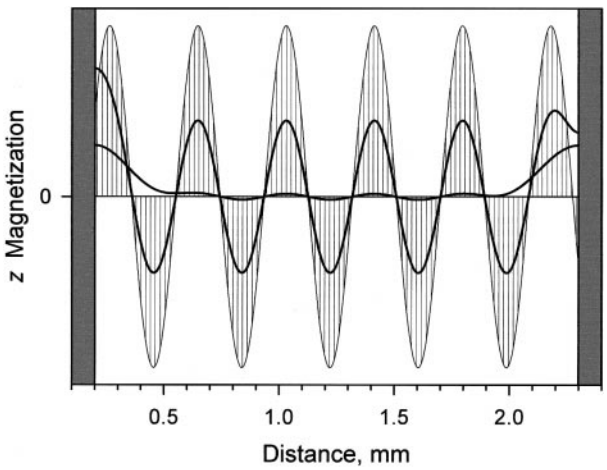

FIG. 8. Decay of a uniform z-magnetization grating in a confined sample according to finite-difference simulations. The thick solid lines show the progress of decay after an evolution time of $\tau = 1.5$ s and $\tau = 7.5$ s, respectively, for an assumed diffusion coefficient of 2.0×10^{-9} m^2 s^{-1}. Substantial edge enhancement is observed near the dark gray bars that symbolize the sample boundaries.

only a phenomenological approximation, not the exact solution of partial differential equations. The second difference between the calculations with Eqs. [5] and [25] is readily seen as a result of adding spatial limitations to the sample volume. Here, diffusion is restricted to the inside of the sample volume, and grating extrema adjacent to the boundaries decay slower than expected by Eq. [5]. At the central conductor, this diffusive edge-enhancement effect (*17*) is especially visible at the profile of $D\tau/(r_{min})^2 = 0.0025$ in Fig. 7a. With increasing evolution time, the area of enhanced z magnetization reaches further into the sample (Fig. 7b). Because of the looser grating adjacent to the sample boundary at $r/r_{min} = 5$, edge enhancement occurs more slowly at the outer wall of the TCD. Here, however, an evaluation with Eq. [5] can lead to negative "apparent" diffusion coefficients, since z magnetization temporarily rises above its initial value (Fig. 7b).

Finite-difference diffusion simulations are not limited to TCDs but can likewise be conducted for other sample geometries or other B_1 gradients. For example, Fig. 8 plots the decay of a uniform magnetization grating of a surface coil as calculated from the finite-difference equation of planar sheets with evenly spaced function values (Eq. [20]). Using this procedure instead of Eq. [2], one can account for the impermeable sample confines, and edge-enhancement effects are clearly shown. Figure 8 also reveals that the edge enhancement depends largely on the phase of the initial grating. At both sample confines ($x_{min} = 0.2$ mm and $x_{max} = 2.3$ mm), however, magnetization first increases and, again, can lead to negative apparent diffusion coefficients if evaluated with the phenomenological approach of Eq. [2].

T_1 Relaxation

Different from the effects of diffusion, T_1 relaxation decays z-magnetization gratings independent of the distances between the grating's extrema. In most cases, the influence of T_1 relaxation is easily calculated by Eq. [5] with the diffusion coefficient set to zero,

$$\mathbf{M}_{z,\tau}(r) = M_{eq}\left[1 - \exp\left(-\frac{\tau}{T_1}\right)\{1 - \mathbf{M}^0_{z,0}(r)\}\right]. \quad [27]$$

where $\mathbf{M}^0_{z,0}(r) = \mathbf{M}_{z,0}(r)/M_{eq}$ is the cosine term of the initial grating as obtained from Eq. [4]. Figure 9 shows z-magnetization profiles after different normalized evolution times, τ/T_1, calculated from Eq. [27]. The oscillations decay as an exponential function of the evolution time, and thermal equilibrium, M_{eq}, is reached after τ/T_1 is greater than 5. After this time, all oscillations disappear and evaluation of the diffusion coefficient is no longer possible.

APPLICATION

Algorithm for Diffusion Coefficient and T_1 Relaxation Time

Conventionally, D, T_1, and M_{eq} would be obtained from a three-parameter least-squares fit of simulated curves to experimental data. Conducting this least-squares fit, however, necessitates a new, complete finite-difference calculation for every refined parameter set, starting with the initial z-magnetization grating. To reduce computer calculation time, we favor an alternative approach that requires only one finite-difference calculation. In this alternative approach, the finite-difference progression steps (Eq. [25]) are carried out using $D\Delta t$, i.e., a normalized time step. To ensure convergence, $D\Delta t$ must obey the Courant criterion derived from Eq. [26]. After each time step (total progression of $HD\Delta t$, where $H = 0$, 1,

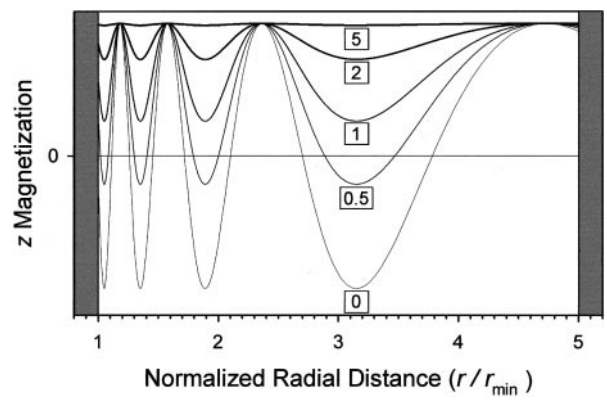

FIG. 9. Decay of a toroid cavity magnetization grating by T_1 relaxation. The solid lines show the remaining grating as calculated for different normalized relaxation times, τ/T_1, as indicated by the labels next to each curve. To exclusively show the effects of relaxation, we neglected diffusion in the calculation.

2, . . .), a linear regression is conducted to determine M_{eq} and T_1,

$$\mathbf{M}_{z,\tau}(r) = b_0 + b_1\mathbf{M}^0_{z,HD\Delta t}(r), \qquad [28]$$

where the coefficients b_0 and b_1 are derived from Eq. [27]:

$$b_0 = M_{eq}\left[1 - \exp\left(-\frac{\tau}{T_1}\right)\right], \quad b_1 = M_{eq}\exp\left(-\frac{\tau}{T_1}\right). \qquad [29]$$

The data points a and z of the finite-difference calculation usually cover irregular sample intervals that are confined by the impermeable boundaries at r_{max} and r_{min}, respectively. The experimental data of a and z, however, represent averaged magnetizations from the entire range covered by these data points. Accordingly, although a and z are included in the finite-difference calculation, except when Δr_a or Δr_z is within the range of the square root of the computer's round-off error (*vide supra*), only values from $a + 1$ to $z - 1$ are used for the linear regression.

The maximum-likelihood criterion of linear regressions is the sum of least-squares deviations of experimental data from simulated data (*34*), i.e., the minimum of the so-called "chi-square" parameter,

$$\chi^2 = \sum_{k=a+1}^{z-1}\left(\frac{M_{z,k,exp} - b_0 - b_1M_{z,k,sim}}{\sigma_k}\right)^2. \qquad [30]$$

where $M_{z,k,exp}$ are magnetizations derived from the experiment, $M_{z,k,sim}$ are simulated data from the finite-difference calculation, and σ_k are experimental standard deviations of the data points k. Usually, standard deviations of NMR intensities are estimated from the noise of the spectrum. Because magnetizations of TCD images, $M_{z,k,exp}$, are derived from division of signal intensities $I_k(r)$ by r_k^2 (*20*), noise increases proportional to k^2 (Eq. [7]). Accordingly, standard deviations in Eq. [30] are $\sigma_k = \sigma_0k^2$, where σ_0 is a constant that is typically unknown and expendable for the linear-regression procedure. It is set to $\sigma_0 = 1$, and standard deviations of $\sigma_k = k^2$ are used in Eq. [30]. However, for the determination of confidence intervals (i.e., for the probabilities of finding the true parameters within a certain range around the best fit), σ_0 must be known and is specified as discussed later.

Since χ^2 is used not only as the maximum-likelihood estimator for M_{eq} and T_1 but also for the diffusion coefficient D, minimum χ^2 values of Eq. [30] must be saved after each finite time step and compared with the minimum χ^2 of the next step. In Fig. 10, typical minimum χ^2 values are plotted versus the number of finite time steps H. The curve shows a minimum that represents the maximum likelihood of all three parameters, M_{eq}, T_1, and D. In addition, the inset shows that the minimum

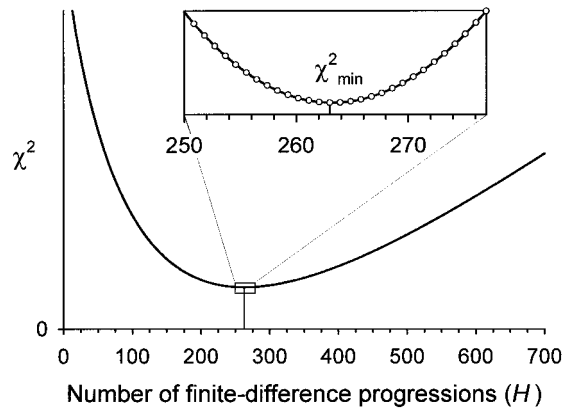

FIG. 10. Plot of the maximum-likelihood parameter χ^2 versus the number of finite-difference progressions H of width $D\Delta t$. The inset shows a detail around the minimum of the curve and exemplifies the individual results by open circles.

is well mapped by the finite-difference step width ($D\Delta t$). It is the only minimum of the curve, because decay of the well-ordered, radially dependent z-magnetization grating by diffusion is irreversible; i.e., it is a process of continuously increasing entropy. With the finite-difference procedure, the entropy process is reproduced stepwise, and χ^2 decreases until the entropies of the calculated grating and the experimental image match. Each additional finite time step increases the predicted amount of entropy and, therefore, further deviates from the entropy of the experimental image.

With Eq. [29], the values $b_{0,min}$ and $b_{1,min}$ leading to the total minimum, χ^2_{min}, are used to extract T_1 and M_{eq} according to

$$M_{eq} = b_{0,min} + b_{1,min}, \quad T_1 = \frac{\tau}{\ln\left(1 + \frac{b_{0,min}}{b_{1,min}}\right)}. \qquad [31]$$

The diffusion coefficient, D, is calculated from the number of finite time steps, H_{min}, used to reach the minimum in the χ^2 curve and from the normalized step width, $D\Delta t$, according to

$$D = \frac{H_{min}(D\Delta t)}{\tau}. \qquad [32]$$

Figure 11 shows the flowchart of a computer program (*35*) for the evaluation of T_1 relaxation and diffusion. At the beginning of the algorithm, experimental parameters, geometric parameters, and the torus factor (A) must be provided for the calculation. With these values, the computer program simulates the normalized, initial grating $\mathbf{M}^0_{z,0}(r)$ produced by the preparation pulse, P1, and determines the data points, k, that fall inside the TCD ($a \geq k \geq z$). Then, the diagonal propagation band matrix P (Eq. [25]) is constructed, and the normalized time step, $D\Delta t$, is calculated from 80% of its maximum value,

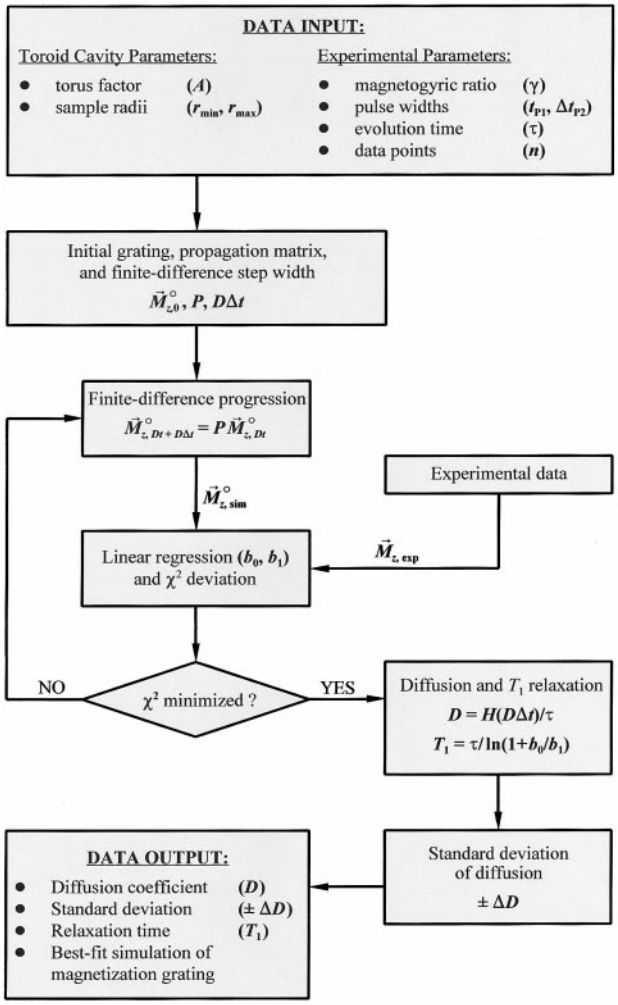

FIG. 11. Flowchart of the computer program for the simultaneous evaluation of the diffusion coefficient (D) and the relaxation time (T_1) by the finite-difference approach.

according to the Courant criterion (Eq. [26]). After the initial application of P, the least-squares parameter χ^2 (Eq. [30]) is calculated from the coefficients b_0 and b_1 of the linear regression (Eq. [29]). The result is stored, and another finite propagation step is conducted. Again, the least-squares parameter χ^2 is evaluated and then compared with the stored χ^2 value. If the latter is smaller, the finite-difference propagation is repeated until the minimum, χ^2_{min}, is found. This minimum is used to calculate M_{eq}, T_1, and D according to Eqs. [31] and [32].

Standard Deviation and Confidence Interval

Confidence intervals of diffusion coefficients derived from the finite-difference approach above are determined as outlined in detail elsewhere (*36*). Accordingly, a standard confidence interval is the region around the calculated diffusion coefficient, in which the true coefficient can be found with 68.3% probability, and is given by a threshold of

$$\chi^2 \leq \chi^2_{min} + 1. \qquad [33]$$

Equation [33] holds for relationships with one dependent variable. For this kind of relationship, the standard confidence interval is equal to the half-height range of a Gaussian distribution and is usually termed the standard deviation. In the plot of χ^2 versus $nD\Delta t$ (e.g., Fig. 10), T_1 and M_{eq} are optimized by the linear regression; consequently, only D is dependent, and Eq. [33] is used to evaluate the standard deviation.

As discussed earlier, experimental standard deviations, σ_k, are typically unknown. With σ_0 set to unity, the calculated χ^2 values are relative numbers that must be adjusted to represent experimental standard deviations. A reasonable and common method for adjusting χ^2 is to assume that the theory of the simulation is complete and accurate. By doing this, however, it must be carefully considered whether the random walk of particles and radially independent longitudinal relaxation are the only effects modifying the magnetization gratings. In particular, relaxation and diffusion during the pulses, pulse imperfections, and off-resonance effects must be negligible. Additionally, accurate representation of the z magnetization by the RFI procedure must be ensured. If these prerequisites hold, deviations between experimental and simulated data at the total minimum, χ^2_{min}, are solely based on experimental deficiencies (e.g., receiver noise), and the standard deviation of experimental data points is recalculated by

$$\sigma_0^2 = \frac{\sum_{k=a+1}^{z-1} \left(\frac{M_{z,k,exp} - b_{0,min} - b_{1,min} M_{z,k,sim}}{k^2} \right)^2}{(z-1) - (a+1) - m}. \qquad [34]$$

where $(z-1)-(a+1)$ reflects the numbers of data points used for the linear regression, and m is the number of parameters determined by the regression; i.e., $m = 2$ for T_1 and M_{eq} (*34*). Accordingly,

$$\sigma_0 = \sqrt{\frac{\chi^2_{min}}{z-a-4}}. \qquad [35]$$

If the relative numbers obtained from Eq. [30] are divided by σ_0 (Eq. [35]), meaningful χ^2 deviations are obtained, and $\chi^2 \leq \chi^2_{min} + 1$ (Eq. [33]) can be used to determine the standard deviation of the diffusion coefficient. Alternatively, a threshold of $\chi^2 = \chi^2_{min} + \sigma_0$ can be applied, and the standard deviation is obtained without rescaling χ^2 data.

Self-Diffusion in Experiments with Acetone

Several experiments have been conducted to generate magnetization gratings in homogeneously filled TCDs and to investigate their subsequent decay during an evolution time τ. The gratings were imaged by an RFI procedure (P2 in Fig. 1), and, from the radially dependent signal intensities, diffusion

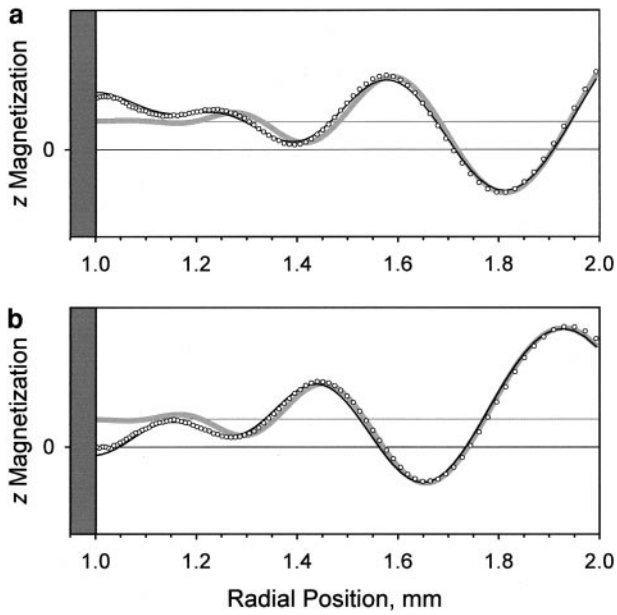

FIG. 12. Plot of experimental RFI intensities (circles) versus radial distance obtained from toroid MAGROFI experiments with acetone ($n = 512$, $\Delta t_{P2} = 12$ μs, $A = 0.6934 \pm 0.0014$ mT mm). Dark gray, vertical bars represent the sample confine at $r_{min} = 1.0$ mm (central conductor). In (a), the preparation pulse width was set to $t_{P1} = 212$ μs, and a positive edge enhancement is observed. In contrast, a negative enhancement is obtained in (b), where the preparation pulse width was set to a slightly different value ($t_{P1} = 195$ μs). In both cases, the finite-difference evaluation (solid lines) correctly reproduces the enhancement effect neglected by the phenomenological approach (heavy gray lines). Thin horizontal lines show baseline offsets caused by T_1 relaxation.

coefficients were determined with the finite-difference procedure. In addition, standard deviations of the coefficients were calculated. Figure 12 shows experimental data (circles) derived from two separate experiments, both conducted with a TCD (inner radius of $r_{min} = 1.0$ mm, outer radius of $r_{max} = 5.0$ mm) completely filled with acetone. In the experiment of Fig. 12a, the MAGROFI pulse sequence was applied with a preparation pulse of $t_{P1} = 212$ μs and an evolution time of $\tau = 1.0$ s, while Fig. 12b resulted from a preparation pulse of $t_{P1} = 195$ μs and an evolution time of $\tau = 1.0$ s. During both experiments, 512 spectra with incrementally increasing pulse widths ($\Delta t_{P2} = 12$ μs) were recorded for the RFI procedure. Although the pulse widths t_{P1} of the two experiments in Fig. 12 were similar and all other parameters were kept the same, Fig. 12a exhibits a positive and Fig. 12b a negative edge enhancement near the central conductor at $r_{min} = 1$ mm. The experimental magnetization was compared to data derived from both the finite-difference approach as described above and the least-squares fit to the phenomenological approach of Eq [5]. The best fits are shown as black and heavy gray solid lines in Fig. 12, respectively. The black lines (finite-difference approach) reveal an excellent agreement between the theory and the experiment. At the inner confine of the sample volume, they correctly reproduce the diffusive edge enhancement and the shift of the magnetization extrema to smaller radii both neglected by Eq. [5] (heavy gray lines in Fig. 12). For acetone at room temperature, the two experiments indicate self-diffusion coefficients of $4.84 \times 10^{-9} \pm 0.22 \times 10^{-9}$ m^2 s^{-1} ($\pm 4.5\%$) and $4.73 \times 10^{-9} \pm 0.15 \times 10^{-9}$ m^2 s^{-1} ($\pm 3.2\%$), and T_1 relaxation times of 5.45 s ($\pm 2.0\%$) and 5.65 s ($\pm 1.8\%$), respectively. The confidence intervals (standard deviations) of both measurements in Fig. 12 cover the value of the acetone self-diffusion coefficient that was determined independently by another technique (*22*).

CONCLUSION

A new calculational method (finite-difference approach) has been developed to accurately simulate molecular diffusion and nuclear spin relaxation in MAGROFI experiments. The new theoretical approach defeats the shortcomings of phenomenological equations, such as neglect of sample geometries with singularities at the confines of the sample volume. Furthermore, since sample geometries are included in the finite-difference approach, it is not necessary to invoke "apparent diffusion coefficients" to describe diffusion at or near spatial singularities, such as sample confines. When using toroid cavity detectors (TCDs) for the experiments, key advantages such as the strong, mathematically well-defined, nonuniform B_1 gradient and the highly reproducible, unique sample geometry are exploited. Further, MAGROFI is a simple two-pulse method that does not require B_0 gradients. Accordingly, the experiments are not affected by B_0 gradient-switching imperfections or B_0 susceptibility mismatches at sample boundaries or interfaces. These important features make the toroid cavity MAGROFI technique combined with our finite-difference calculations one of the most accurate NMR methods for determining molecular self-diffusion in fluids.

In addition to the determination of self-diffusion and diffusion in homogeneous mixtures, the finite-difference approach presented here makes it possible to include concentration or spatially dependent diffusion measurements. For simplicity in our discussion of the finite-difference equations, this feature has not explicitly been addressed here. However, a propagation matrix similar to the one in Eq. [23] can be derived from the finite-difference expression of Eq. [18], where each data point k maintains an individual diffusion coefficient D_k.

In addition to the optimization of D, T_1, and M_{eq}, we have attempted to incorporate an optimization of the torus factor, A, into the evaluation of MAGROFI data sets. However, several local minima occurred in the plot of χ^2 versus $HD\Delta t$, depending on the magnetization-grating profile. As a consequence, the standard deviations increased significantly (*37*). Therefore, we recommend that A be determined separately from a regular toroid cavity RFI measurement. This should be interleaved with the diffusion measurement to ensure equal experimental conditions.

Because diffusion is accurately described not only inside a homogeneously filled sample volume but also at singularities, the finite-difference approach is useful for investigating diffusive mass transport between phases (e.g., liquids swelling polymers) or through membranes (e.g., in osmosis). When the central conductor is used as a working electrode (*38, 39*), the method introduced here can help to extract transport numbers that are important for electrochemical studies or, combined with the ability of the RFI procedure to retain chemical-shift information, it can be employed to analyze diffusion-limited chemistry on the surface of an electrode. All the experiments suggested above can easily be conducted under high pressure and high temperature, since TCDs are easily implemented into NMR autoclave probes (*20, 38*). In future work, we plan on using this new technique for diffusion measurements under supercritical conditions (e.g., in supercritical CO_2).

ACKNOWLEDGMENTS

This work was supported by the U.S. Department of Energy, Division of Chemical Sciences, Office of Basic Energy Sciences, under Contract W-31-109-Eng-38, and by the German Research Foundation (Deutsche Forschungsgemeinschaft) under Program Wo 613/2-1. We thank Prof. Dr. G. Woelk, Technical University of Aachen, Germany, for many helpful discussions and for bringing the digital Beuken model to our attention. We appreciate the assistance of J. Koehler, University of Bonn, Germany, for helping us to understand several details of the finite-difference procedure. Parts of this article were presented in preliminary form at the 4th International Conference on Magnetic Resonance Microscopy and Macroscopy, Albuquerque, New Mexico, September 1997 (*40*).

REFERENCES

1. C. T. Costello and A. H. Jeske, Iontophoresis: Applications in transdermal medication delivery, *Phys. Ther.* **75,** 554–563 (1995).
2. N. N. Byl, The use of ultrasound as an enhancer for transcutaneous drug delivery: Phonophoresis, *Phys. Ther.* **75,** 539–553 (1995).
3. P. Stilbs, Fourier transform pulsed-gradient spin-echo studies of molecular diffusion, *Progr. NMR Spectrosc.* **19,** 1–45 (1987).
4. P. T. Callaghan, "Principles of Nuclear Magnetic Resonance Microscopy," p. 162, Clarendon Press, Oxford (1991).
5. G. S. Karczmar, D. B. Twieg, T. J. Lawry, G. B. Matson, and M. W. Wiener, Detection of motion using B_1 gradients, *Magn. Reson. Med.* **7,** 111–116 (1988).
6. D. Canet, B. Diter, A. Belmajdoub, J. C. Boubel, and K. Elbayed, Self-diffusion measurements using a radiofrequency field gradient, *J. Magn. Reson.* **81,** 1–12 (1989).
7. V. Blechta and J. Schraml, Effect of relaxation and diffusion on spatially inhomogeneous magnetization. Application to self-diffusion measurements employing a radiofrequency field gradient, *J. Magn. Reson.* **87,** 601–604 (1990).
8. D. Bourgeois and M. Decorps, A B_1-gradient method for the detection of slow coherent motion, *J. Magn. Reson.* **91,** 128–135 (1991).
9. R. Dupeyre, Ph. Devoulon, D. Bourgeois, and M. Decorps, Diffusion measurements using stimulated rotary echoes, *J. Magn. Reson.* **95,** 589–596 (1991).
10. R. Kimmich, B. Simon, and H. Köstler, Magnetization-grid rotating-frame imaging technique for diffusion and flow measurements, *J. Magn. Reson. A* **112,** 7–12 (1995).
11. D. I. Hoult, Rotating frame zeugmatography, *J. Magn. Reson.* **33,** 183–197 (1979).
12. J. L. Bowers, P. M. Macdonald, and K. R. Metz, Rapid chemical-shift selective MR imaging with use of radio-frequency field gradients, *Radiology* **173**(P), 227 (1989).
13. D. Boudot, D. Canet, and J. Brondeau, Spatial labeling by a radio-frequency field gradient. DANTE-Z profile, probed by one-dimensional nutation imaging, *J. Magn. Reson.* **87,** 385–394 (1990).
14. K. R. Metz, J. P. Boehmer, J. L. Bowers, and J. R. Moore, Rapid rotating-frame imaging using an RF pulse train (RIPT), *J. Magn. Reson. B* **103,** 152–161 (1994).
15. J. J. H. Ackerman, T. H. Grove, G. G. Wong, D. G. Gadian, and G. K. Radda, Mapping of metabolites in whole animals by ^{31}P NMR using surface coils, *Nature* **283,** 167–170 (1980).
16. D. I. Hoult and R. E. Richards, The signal-to-noise ratio of the nuclear magnetic resonance experiment, *J. Magn. Reson.* **24,** 71–85 (1976).
17. B. Pütz, D. Barsky, and K. Schulten, Edge enhancement by diffusion: Microscopic magnetic resonance imaging of an ultrathin glass capillary, *Chem. Phys. Lett.* **183,** 391–396 (1991).
18. M. Valtier, F. Humbert, and D. Canet, Maps of self-diffusion coefficients by radiofrequency field gradient NMR microscopy, *J. Magn. Reson.* **141,** 7–17 (1999).
19. F. Humbert, M. Valtier, and D. Canet, Restricted molecular diffusion in the vicinity of a reflective wall as probed by NMR measurements using radio-frequency field gradients, *Chem. Phys. Lett.* **302,** 1–6 (1999).
20. K. Woelk, J. W. Rathke, and R. J. Klingler, The toroid cavity NMR detector, *J. Magn. Reson. A* **109,** 137–146 (1994).
21. K. Woelk, R. E. Gerald II, R. J. Klingler, and J. W. Rathke, Imaging diffusion in toroid cavity probes, *J. Magn. Reson. A* **121,** 74–77 (1996).
22. Landolt-Börnstein, "Zahlenwerte und Funktionen aus Physik, Chemie, Astronomie, Geophysik und Technik," Vol. 2, "Eigenschaften der Materie in ihren Aggregatzuständen," Part 5(a), "Transportphänomene 1, Viskosität und Diffusion," 6th ed., p. 592, Springer-Verlag, Berlin (1969), and references therein.
23. K. Woelk, J. W. Rathke, and R. J. Klingler, Rotating-frame NMR microscopy using toroid cavity detectors, *J. Magn. Reson. A* **105,** 113–116 (1993).
24. J. Crank, "The Mathematics of Diffusion," p. 187, Oxford Univ. Press, Oxford (1967); J. Crank, "The Mathematics of Diffusion," 2nd ed., p. 141, Oxford Univ. Press, Oxford (1975).
25. S. Zandstra and A. J. Bovy, "Literature with Respect to Theory, Design and Applications of the Beuken Model to the Analysis of Transient Heat Flow Problems," 2nd ed., Library Technical University Delft, The Netherlands (1963).
26. J. Crank, "The Mathematics of Diffusion," p. 213, Oxford Univ. Press, Oxford (1967). [Not mentioned in the 2nd edition, 1975]
27. S. W. Feldberg, Digital simulation: A general method for solving electrochemical diffusion-kinetic problems, *in* "Electroanalytical Chemistry" (A. J. Bard, Ed.), p. 202, Dekker, New York (1969).
28. C. L. Beuken, "Wärmeverluste bei periodisch-betriebenen elektrischen Öfen, eine neue Methode zur Vorausbestimmung nichtstationärer Wärmeströmungen," Dissertation, Sächs. Bergakademie Freiberg, Germany (1936).
29. G. Woelk, Ein universelles Beukenmodell für Lehre und Forschung, *Industrieanzeiger* **93,** 2343 (1971).

30. H. Köhne and G. Woelk, The digital Beuken model—A method for determining non-stationary heat-conduction processes, *Elektrowärme Int.* **27,** 302–308 (1969).

31. J. Crank, "The Mathematics of Diffusion," 2nd ed., p. 157, Oxford Univ. Press, Oxford (1975).

32. P. W. Atkins, "Physical Chemistry," 3rd ed., p. 681, Oxford Univ. Press, Oxford (1986).

33. R. Courant, K. Friedrichs, and H. Lewy, Über die partiellen Differentialgleichungen der Mathematischen Physik, *Math. Ann.* **100,** 32–74 (1928).

34. W. H. Press, S. A. Teukolsky, W. T. Vetterling, and B. P. Flannery, "Numerical Recipes in C," 2nd ed., pp. 660–661, Cambridge Univ. Press, Cambridge (1992).

35. The computer program, written in C, is available from the author (B.L.J.Z.) upon request.

36. W. H. Press, S. A. Teukolsky, W. T. Vetterling, and B. P. Flannery, "Numerical Recipes in C," 2nd ed., pp. 692–698, Cambridge Univ. Press, Cambridge (1992).

37. E. Lehnhof, "Bestimmung des Torusfaktors für die Nutationsbildgebung im Torus-Hohlraumdetektor," Thesis (Diplomarbeit), University of Bonn, Germany (1997).

38. J. W. Rathke, R. J. Klingler, R. E. Gerald II, K. W. Kramarz, and K. Woelk, Toroids in NMR spectroscopy, *Prog. NMR Spectrosc.* **30,** 209–253 (1997).

39. R. E. Gerald II, R. J. Klingler, J. W. Rathke, G. Sandí, and K. Woelk, *In situ* imaging of charge carriers in an electrochemical cell, *in* "Spatially Resolved Magnetic Resonance" (P. Blümler, B. Blümich, R. Botto, and E. Fukushima, Eds.), pp. 111–119, Wiley–VCH, Weinheim (1998).

40. K. Woelk, B. L. J. Zwank, J. Bargon, R. J. Klingler, R. E. Gerald II, and J. W. Rathke, Imaging diffusion with non-uniform B_1 gradients, *in* "Spatially Resolved Magnetic Resonance" (P. Blümler, B. Blümich, R. Botto, and E. Fukushima, Eds.), pp. 103–110, Wiley–VCH, Weinheim (1998).